

Convective dissolution of CO₂ in water and salt solutions

C. Thomas, S. Dehaeck, A. De Wit*

Université libre de Bruxelles (ULB), Nonlinear Physical Chemistry Unit, CP231, 1050 Brussels, Belgium



A B S T R A C T

Dissolution of CO₂ into saline aquifers can lead to the development of buoyancy-driven convection in the brine which enhances the efficiency of CO₂ transfer. We analyze here experimentally the onset, development and dynamic properties of such convective fingering of CO₂ into water, Antarctic water and in NaCl salt solutions of various concentrations to study the influence of varying the salt concentration on the buoyancy-driven convective dynamics. The convective dissolution pattern is visualized with the help of a schlieren imaging system sensitive to density gradients in the solution. We quantify the growth of convective fingers by performing, among others, a Fourier analysis of the pattern formation at early times and qualitatively study the nonlinear spatio-temporal dynamics at later times. In agreement with theoretical predictions, we find that increasing the salt concentration hinders the development of the instability as it delays the onset of convection, increases the wavelength of the convective pattern, decreases the growth rate and velocity of fingers as well as their interactions. Our experimental results provide quantitative data that should help the benchmarking of theoretical studies.

1. Introduction

Considering the large increase of atmospheric CO₂ concentration during the last decades and its dramatic implications on climate change, the interest for techniques mitigating greenhouse gas emissions is growing. Among these, CO₂ Capture and Sequestration (CCS) in geological reservoirs is receiving increased attention (Metz et al., 2005; International Energy Agency, 2016; Pachauri and Meyer, 2014). Explicitly, CO₂ is captured at the exit of power plants and is transported through pipelines to storage sites where it is injected in underground reservoirs to be separated from the atmosphere for a long period of time. In CCS scenarios, one of the main options is to inject CO₂ into saline aquifers. Upon injection into these deep geological formations, the less dense liquid or supercritical CO₂ rises above the brine, in which it next slowly dissolves over time. The dissolution of CO₂ in the aqueous phase increases its density, resulting in a local stratification of denser CO₂-enriched brine overlying less dense brine, which may induce a buoyancy-driven convective instability after some time. Consequently, denser CO₂-rich brine fingers sink towards the bulk of the reservoir. This convective instability is a favorable process for CO₂ sequestration as it accelerates dissolution and mixing of CO₂ into the aqueous phase, reducing the time needed to safely store CO₂ in the aquifer (Ennis-King and Paterson, 2002, 2005; Hassanzadeh et al., 2005, 2006; Riaz et al., 2006; Yang and Gu, 2006; Elenius and Johannsen, 2012; Seyyedi et al., 2014; Emami-Meybodi et al., 2015). Saline aquifers are well distributed

around the world and their physico-chemical characteristics, such as permeability, salinity, temperature, pressure and composition differ considerably from one reservoir to the other. For example, salinities can range from 0.08 M to 5.13 M (5–300 g/l) (Bour and Thoraval, 2010). It is therefore important to understand the impact of those salinity changes on the efficiency of CO₂ sequestration if quantitative predictions of CO₂ mixing times in the aquifer and storage volumes are to be predicted.

Theoretical studies of CO₂ convective dissolution typically consider a two-dimensional idealized porous medium with a two-layer stratification of pure CO₂ above water or brine (Ennis-King and Paterson, 2005; Ennis-King et al., 2005; Riaz et al., 2006; Hassanzadeh et al., 2007; Neufeld et al., 2010; Pau et al., 2010; Hidalgo et al., 2012; Emami Meybodi and Hassanzadeh, 2013; Loodts et al., 2014b; Emami-Meybodi, 2017). By means of linear stability analysis or nonlinear simulations, theoretical works have determined properties of the fingering pattern generated by CO₂ convective dissolution into water or brine, such as the characteristic onset time, growth rate, length and wavelength of the fingers for given physical properties of the reservoir. Among these studies, Loodts et al. (2014b) have investigated the impact of salinity, temperature and pressure on the short-time development of density-driven instability. In particular, they have shown that increasing salt concentration has a stabilizing effect on convection. In parallel, Slim (2014) has described numerically the successive convective dynamic regimes developing upon CO₂ dissolution in brine. The

* Corresponding author.

E-mail address: adewit@ulb.ac.be (A. De Wit).

ultimate goal of such theoretical studies is to obtain predictions on storage capacities, dissolution rates, and time scales governing CO₂ convective dissolution in storage sites. However, despite the crucial need to benchmark such theoretical models, very few attempts have been made to compare quantitatively theoretical predictions with experimental results. This comparison is indeed difficult for two main reasons: on one side, theoretical results, which are usually presented in dimensionless variables, do not always consider the range of parameters accessible to experiments, and on the other side very few experimental studies provide precise quantitative data that can be used to benchmark theoretical models. Qualitative comparisons between experimental and theoretical results are nevertheless generally satisfying, which suggests promising results if further efforts are made to confront theory and experiments.

At the laboratory scale, experimental studies have been carried out for instance with pressure, volume, temperature (PVT) cells or Hele–Shaw cells. PVT cells used for CO₂ convective dissolution experiments consist in high-pressure cylindrical vessels in which pressure decay and mass transfer rates of dissolved CO₂ into brine can be measured (Yang and Gu, 2006; Farajzadeh et al., 2007, 2009; Firoozabadi and Cheng, 2010; Khosrokhavar et al., 2014; Seyyedi et al., 2014; Karimaie and Lindeberg, 2017). Recently, Seyyedi et al. (2014) and Khosrokhavar et al. (2014) have measured CO₂ dissolution rates in such PVT cells and have shown that increasing brine salinity reduces the Rayleigh number of the system and diminishes the mass transfer of CO₂ in brine. However, those reactors do not allow the visualization and characterisation of the fingering dynamics generated by CO₂ convective dissolution.

Visualization of convective dissolution dynamics are typically carried out in vertical Hele–Shaw cells, composed of two transparent plates separated by a small gap. Such cells provide a quasi two-dimensional environment to follow by direct optical imaging the development of convective patterns generated by CO₂ dissolution in the aqueous phase (Kneafsey and Pruess, 2010, 2011; Backhaus et al., 2011; Soroush et al., 2012; Taheri et al., 2012; Faisal et al., 2013, 2015; MacMinn and Juanes, 2013; Slim et al., 2013; Tsai et al., 2013; Loodts et al., 2014a; Outeda et al., 2014; Seyyedi et al., 2014; Thomas et al., 2016; Vreme et al., 2016). Some studies have visualized the convective fingering generated by the dissolution of acidic CO₂ in water or in brine with the help of color indicators (Kneafsey and Pruess, 2010, 2011; Faisal et al., 2013, 2015; Outeda et al., 2014; Seyyedi et al., 2014; Vreme et al., 2016). Using bromocresol green, Kneafsey and Pruess have first attempted to characterize precisely CO₂ convective fingering in a Hele–Shaw cell by measuring the onset time of convection, the number and averaged length of fingers, and the area of the pH-depressed zone (Kneafsey and Pruess, 2010). They also performed pressure decay experiments to evaluate the total mass of dissolved CO₂ in systems having different permeabilities, pressures and salinities (Kneafsey and Pruess, 2011). In a similar study, Outeda et al. (2014) analyzed the temporal evolution of the mixing zone as well as dispersion curves and growth rate of convective patterns for different CO₂ pressures and various color indicator concentrations. Recently, Vreme et al. (2016) performed a quantitative analysis of the fingering pattern developing upon CO₂ dissolution in Hele–Shaw cells with different pressures and gap widths in order to determine the range of Rayleigh numbers in which the Darcy porous medium model is valid. By means of Fourier analysis, they measured characteristic wavenumbers, growth rates and onset times of the fingering pattern visualized with fluorescein.

Beyond the fact that the number of experimental studies remains limited, another issue is the fact that the width of the system often remains limited in previous studies, such that only a few fingers can be followed in time with some possible lateral boundary effects. Moreover, it has been shown that the addition of an indicator in the aqueous solution can potentially affect the development of the convective dynamics (Almarcha et al., 2010; Kuster et al., 2011; Outeda et al., 2014; Thomas et al., 2015). As detailed below, color indicators also miss

evaporation-driven convection instabilities developing in non-saturated gas systems. Experiments using these indicators for visualization purposes should therefore be interpreted with caution. Optical imaging techniques, like interferometry (Wylock et al., 2011, 2014) or schlieren set-ups (Loodts et al., 2014a; Thomas et al., 2015, 2016) have been shown to be useful tools to image convective dissolution without interfering with the dynamics in reactive systems. Experiments with dissolution of other solutes such as KMnO₄ (Slim et al., 2013) or NaCl (Rasmusson et al., 2017) have been also performed.

The visualization and characterization of CO₂ convective fingers in pure water and salt solutions is however still missing. Moreover, to the best of our knowledge, no experimental study has analyzed the developed nonlinear convective regimes predicted by Slim (2014) for dissolution of CO₂ in water or in brine. In addition, although various experimental works focused on the effect of varying pressure and permeability on CO₂ convective dissolution, very few of them investigated how salinity impacts the development of the convective instability.

In this context, we provide here a detailed experimental quantitative analysis of the growth of the convective instability developing upon CO₂ dissolution in water and in salt solutions. With a schlieren imaging system highly sensitive to density gradients, we follow and compare the spatio-temporal development of the density-driven convection generated by dissolution of gaseous CO₂ in pure water, in Antarctic water and in water containing NaCl in concentration 0.5–5 M at atmospheric pressure (1 bar) in a Hele–Shaw cell. The cell is particularly long and large such that more than 40 fingers can develop at onset in the aqueous phase, allowing to follow the central zone in space and time in the nonlinear regime without any side effect. Fingering characteristics are measured to provide quantitative information regarding the characteristic onset time, growth rate, wavelength and velocity of fingers at early times. We also present space-time maps providing a general overview of the long time nonlinear fingering dynamics near the interface in water and in solutions of increasing salinity. Finally, we compare our experimental results to existing experimental results and theoretical predictions.

The paper is organized as follows. First, we describe in Section 2 the experimental set-up and the protocol followed to perform experiments. In Section 3, we describe qualitatively the fingering dynamics developing in water and in salt solutions. Then, the characteristics of the dynamics are measured quantitatively in Section 4. Finally, we discuss and summarize the results in Sections 5 and 6, respectively.

2. Experimental set-up

Solutions of NaCl (58.44 g/mol, purity \geq 99%, Sigma-Aldrich) are prepared with deionised water. Mineral water samples were also tested to observe the behaviour of the system in a genuine environment. For this purpose, potable groundwater like Spa[®] and Hepar[®] commercial mineral waters were used (see composition in Table 1). In addition, samples of Antarctic water collected in the Weddell sea during the ISPOL 2004 mission at a depth of 30 m were also considered. The Antarctic water sample is not filtered and the salinity measured by means of a Guidline Autosol salinometer is $(34.544 \pm 0.002)\%$. In order to compare the results obtained in Antarctic water with other salt

Table 1
Composition of Spa[®] and Hepar[®] commercial mineral waters (mg/l).

	Spa	Hepar
HCO ₃ ⁻	15	383.7
Na ⁺	3	14.2
Ca ²⁺	4.5	549
Mg ²⁺	1.7	119
SO ₄ ²⁻	4	1530

Table 2

Concentrations, viscosities and densities of aqueous solutions at 1 bar, like in this study. The temperature T at which the density measurement was performed is given in the last column. The asterisk $^{\circ}$ stands for Antarctic water. Note that $1 \text{ cP} = 10^{-3} \text{ Pa s}$.

[NaCl] (mol/l)	[NaCl] (g/l)	Viscosity (cP)	Density (g/l)	Temperature ($^{\circ}\text{C}$)
0.00	0.00	1.10	998.5	20.1
0.50	29.22	1.11	1018.1	21.0
0.59 $^{\circ}$	34.54	1.20	1023.7	22.2
1.00	58.44	1.21	1038.1	18.9
1.50	87.66	1.27	1058.1	19.2
2.00	116.88	1.32	1077.5	20.3
2.50	146.10	1.40	1096.0	19.0
3.00	175.32	1.50	1114.2	19.8
5.00	292.20	1.97	1185.4	19.8

solutions of NaCl, we roughly consider that the only species in solution is NaCl. The corresponding NaCl concentration of the Antarctic water samples is therefore 0.59 M NaCl (34.544 g/l). A summary of measured concentrations, densities and viscosities of the aqueous solutions used is given in Table 2. Experiments are carried out at room temperature ($\sim 20^{\circ}\text{C}$). The partial pressure of the injected gaseous CO_2 is larger than 0.995 bar.

Experiments are performed in a Hele–Shaw cell composed of two 6 mm thick flat glass plates separated by a thin gap and mounted in a metallic frame that presses the plates against each other with uniform pressure (cf. Fig. 1 of Thomas et al., 2016). A silicone rubber spacer of thickness 1 mm is placed between the plates to give a gas and water-tight inner space between the plates of width 165 mm \times 210 mm height and 1 mm thickness. As depicted in Fig. 1, the shape of the spacer is designed to uniformly inject gaseous CO_2 in the upper part of the cell and to continuously evacuate the excess of CO_2 in order to keep the inside of the cell at atmospheric pressure.

The experimental protocol is as follows. First, gaseous N_2 starts flowing inside the cell at a rate of a few hundreds of milliliters per minute. Then, while N_2 continues to flow, 18 ml of aqueous solution is injected through the injection hole situated at the bottom of the cell up to a height of 10 cm. Then, the valve between the gas tanks is switched to replace the flow of N_2 by CO_2 keeping the same flow rate. The initial time $t = 0 \text{ s}$ corresponds to the time at which N_2 is replaced by CO_2 . Gaseous CO_2 starts to invade the cell a few seconds after the beginning of experiment. Each experiment is repeated at least 5 times with the

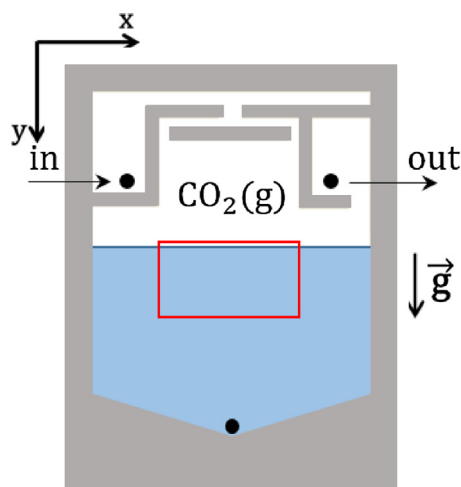


Fig. 1. Schematic of the Hele–Shaw cell (front). The spacer is designed to inject gaseous CO_2 uniformly above the aqueous solution shown in blue. The red rectangle represents the area imaged during experiments. (For interpretation of the references to color in this figure legend, the reader is referred to the web version of the article.)

same initial conditions.

A schlieren technique is used to image the convective patterns in the aqueous solution (Settles, 2001). This technique is sensitive to refractive index gradients and relies on the fact that CO_2 dissolution changes the density of water, which in turn influences its refractive index. This allows us to follow the density-driven dynamics in real time nonintrusively. As depicted in Fig. 2, our schlieren system consists in the alignment of a light source (fiber optic illuminator); two achromatic lenses of diameter 15 cm with 1.5 m focal length, between which the Hele–Shaw cell is placed; a horizontal knife edge (visualization of vertical gradients), and a monochromatic camera to record the experiment. To improve contrast and spatial resolution, images are recorded in 12 bits and a 200 mm micro-Nikkor objective is used to focus on a central 8.8 cm \times 4.7 cm field of view. As this observation window is centered around 50% of the aqueous phase in the middle of the cell, the roughly 20 initial fingers shown in experimental figures are not perturbed by side effects. The rate of frame acquisition is adapted to the speed at which the instability develops. For instance, the frame rate is 1 fps for water experiments whereas it is 0.1 fps for NaCl 5 M where the dynamics is considerably slower.

An important point in the experimental protocol is that gases in contact with the aqueous interface (N_2 and CO_2) have to be saturated with water vapor. This can be achieved by injecting gases in a bottle partially filled with water before their introduction in the cell. This step is mandatory because it prevents the evaporation of the aqueous solution in non-saturated gases, which also triggers convective motions below the interface. This evaporation-driven instability is absent in pure water but becomes very strong when increasing salt concentration (Thomas, 2017). Note that this evaporation related convection can be detected with an optical imaging system but not with color indicators as the density of the solution is affected by evaporation but not the pH.

At ambient conditions, the density increase following the dissolution of gaseous CO_2 in pure water is relatively small (in the order of 0.3 g/l) and the associated gradients of refractive index are weak and difficult to detect. As a result, the sensitivity of our schlieren set-up needed to be optimized. As detailed in Settles (2001), this can be achieved by increasing the cut-off by the knife edge and the exposure time of the camera. In this way, one sacrifices measurement range for sensitivity but this is acceptable here. Another important step to increase sensitivity is to subtract a reference image taken before the experiment starts. This allows to remove initial variations coming from the optical set-up and Hele–Shaw cell inhomogeneities. Finally, note that due to vibrations (and the high sensitivity of our set-up), a flickering is sometimes observed in the videos as the average intensity of the image changes from one picture to another. However, as this results in a uniform offset per image, this can efficiently be dealt with in post-processing.

The dimensionless Rayleigh number characterizing the system is defined here as

$$R_a = \frac{\Delta\rho g a^3}{(12)^{3/2} \phi \mu D_{\text{CO}_2}} \quad (1)$$

It depends on 6 parameters: $\Delta\rho$ the density difference between the CO_2 -rich solution in concentration A_0 and the initial solution with no CO_2 , g the gravitational acceleration, the gap width $a = 1 \text{ mm}$ of our Hele–Shaw cell, ϕ the porosity (equal to 1 for a Hele–Shaw cell), the viscosity μ of the brine and the diffusion coefficient D_{CO_2} of CO_2 . Rayleigh numbers as well as typical experimental values of some key parameters influencing the dynamics for systems of various salinities are summarized in Table 3. In our experimental conditions, the Rayleigh number decreases slightly as the brine salinity increases. Indeed, $R_a = 38.7$ for the water system whereas it equals 33.8 for the highest NaCl concentration.

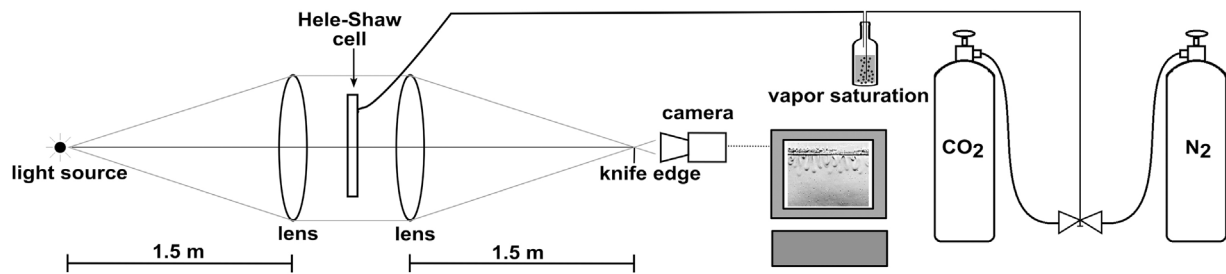


Fig. 2. Schematic of the experimental set-up.

3. Qualitative development of CO₂ convective instability

Let us begin with the qualitative comparison of the instability generated by CO₂ dissolution in water and in salt solutions.

3.1. Development of density-driven fingering

Experiments of CO₂ dissolution were performed in pure water, two different mineral waters, Antarctic water, and in solutions of NaCl 0.5 M, 1 M, 1.5 M, 2 M, 2.5 M, 3 M and 5 M. An example of schlieren images obtained during the development of the density-driven convective fingering in water, Antarctic water, and in NaCl 2 M is shown in Fig. 3. Videos provided in the Supplementary Material allow to fully appreciate the development of the different dynamics over time.

In pure and mineral waters and in solutions containing low concentrations of salt, the development of the density-driven fingering is similar to what has been described in previous studies (Kneafsey and Pruess, 2010, 2011; Faisal et al., 2013, 2015; Outeda et al., 2014; Vreme et al., 2016). During the first minutes following the introduction of gaseous CO₂ in the upper part of the cell, a denser layer develops below the gas–water interface. This layer grows diffusively over time as long as convection does not occur. After a few minutes, the thickened diffusive layer becomes unstable and starts to deform, marking the onset time of convection. Next, the convective deformation amplifies and many finger-like plumes form, sinking downwards from the interface. Fingers are characterized by a thin base and a large tip that extends over time. The more contrasted parts of fingers are their core and tip, meaning that this is where the largest vertical density gradients are found. During progression towards the bulk of the solution, fingers grow, elongate and enlarge. Some finger merging is also observed. Finally, they progressively lose their contrast and fade in time due to the

decrease of density gradients resulting from diffusion and convective mixing. The largest contrast differences are seen near the interface which indicates that density gradients are strongest in this region.

From our observations, no difference was noticed between experiments using deionised water and mineral waters (Spa® and Hepar®). Therefore the results concerning these potable waters will not be discussed any further as no relevant specific information could be obtained from those experiments. On the contrary, increasing salt concentration has a strong negative impact on the development of the convective instability. First, Fig. 3 shows that fingers appear later in 2 M NaCl solutions than in pure water. The development of convective fingering is slower if the salinity of the solution is increased. It is also clear that less fingers are present and that they interact less in NaCl 2 M than in less saline solutions. No convection was observed in NaCl 3 M and 5 M but only the growth of a diffusive boundary layer during the time period considered (2 h and 5 h, respectively). Finally, we note that the reproducibility of experiments decreases with increasing salinity. In some cases, several experiments were performed in addition to the five initial experiments to strengthen the results.

3.2. Space-time maps

To study the movement of fingers and nonlinear dynamics in the course of time, we analyze space-time maps of the location of finger bases near the interface during a 2 h experiment. To do so, we plot pixel intensities along a horizontal line 3 mm below the gas–liquid interface as a function of time running downwards. Such a diagram offers a general overview of finger movements, births and interactions during the course of time.

Fig. 4 shows examples of typical space-time maps of CO₂ dissolution in water, Antarctic water and in NaCl 1 M and 2 M solutions. Globally,

Table 3

Typical experimental values at 20 °C for various concentrations in NaCl in mol/l of some key parameters influencing the dynamics. The partial pressure of CO₂ is 1 bar. A₀ and D_{CO₂} are the solubility and diffusion coefficient of CO₂. ρ₀, Δρ, μ, u_c, l_c, t_c, R_a, t_{onset}, λ and k denote respectively the solution density, the density difference between the CO₂-rich solution in concentration A₀ and the initial solution with no CO₂, the solution viscosity, the characteristic speed, length and time scales, the Rayleigh number and the onset time, wavelength and wavenumber measured experimentally. α_{CO₂} = 0.00815 l/mol is the solutal expansion coefficient of CO₂ in pure water; φ = 1 is the typical porosity of a Hele–Shaw cell; g = 9.81 m/s² is the gravitational acceleration; and κ = a²/12 = 8.33 10^{−8} m² represents the permeability of our Hele–Shaw cell having a gap width a = 10^{−3} m. The values of viscosity μ (Pa s) and initial density ρ₀ (g/l) were measured experimentally (see Table 2).

		Water	1 M	2 M	3 M	5 M
A ₀ (mol/l)	From Henry's law and Ref. (Loodts et al., 2014b)	0.039	0.032	0.027	0.023	0.016
D _{CO₂} (10 ^{−9} m ² /s)	1.75 10 ^{−9} e ^(−0.229[NaCl]) (Sell et al., 2013)	1.75	1.39	1.11	0.88	0.56
ρ ₀ (g/l)	Measured	998.5	1038.1	1077.5	1114.2	1185.4
Δρ (g/l)	ρ ₀ α _{CO₂} A ₀	0.32	0.27	0.24	0.21	0.16
μ (10 ^{−3} Pa s)	Measured	1.10	1.21	1.32	1.5	1.97
u _c (10 ^{−4} m/s)	Δρgκ/μ	2.38	1.82	1.49	1.14	0.66
l _c (10 ^{−6} m)	φ D _{CO₂} /u _c	7.35	7.64	7.45	7.72	8.49
t _c (s)	φ ² D _{CO₂} /u _c ²	0.031	0.042	0.050	0.068	0.129
R _a	Δρ g a ³ /(12) ^{3/2} φμ D _{CO₂}	38.7	38.4	38.1	36.9	33.8
t _{onset} (s)	Standard deviation	133	272	450	–	–
λ (10 ^{−3} m)	Fourier analysis	3.8	3.9	5.7	–	–
k (10 ³ m ^{−1})	2π/λ	1.7	1.6	1.1	–	–

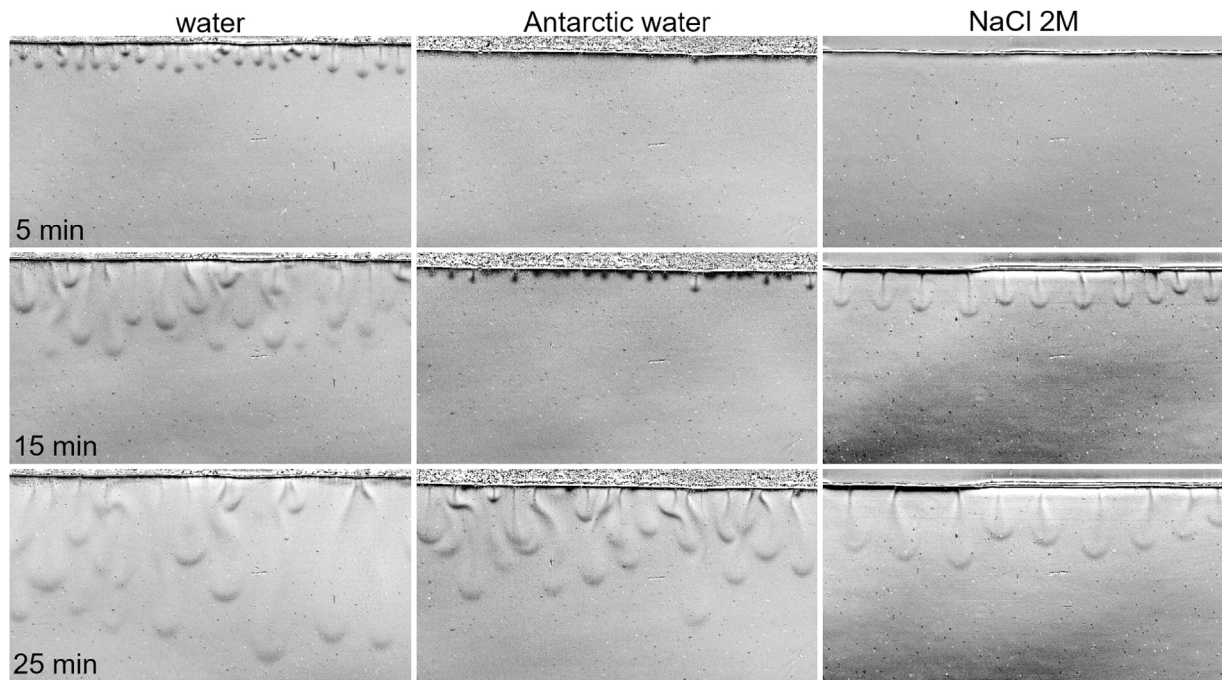


Fig. 3. Time series of the development of the convective instability generated by the dissolution of gaseous CO_2 in water, Antarctic water and in 2 M NaCl solution. The partial pressure of CO_2 is 1 bar. The field of view is $8.8 \text{ cm} \times 4.7 \text{ cm}$.

the fingering phenomenology is similar in all experiments, even if the time scales of the successive convective regimes vary from one map to another.

First, we note in Fig. 4 that the initial wavelength λ of fingers increases with salinity with respectively 22, 19, 19 and 15 fingers being observed at the onset of convection in pure water, Antarctic water, 1 M and 2 M NaCl solutions. The time at which they appear is also delayed when the salt concentration increases which points to stabilisation of convective dissolution in the presence of brine.

As described by Slim (2014), different stages of convection can be identified. During a 2 h experiment, we observe all those before the saturation of the system (shut-down regime), namely the linear growth, the nonlinear regime, and the reignition phase.

At the onset of convection, we first observe the emergence of fingers featuring a vertical downwards growth independently from each other with very small lateral movements. After some time, fingers start to interact with each other, which corresponds to the beginning of the nonlinear regime where lateral movements of finger bases become significant and some fingers eventually merge with their neighbours. This merging, which is initiated at the base of fingers, can sometimes involve three fingers or more at the same time. Once fingers have merged, the mean distance between two of them increases. A reignition phase then starts (Slim et al., 2013; Slim, 2014; Loodts et al., 2017) in which new fingers form at the gas–water interface between existing primary fingers. Those new small fingers, or “proto-fingers”, appear close to primary well-developed fingers towards which they are strongly attracted and in which they are eventually absorbed. This is clearly visible on space-time maps (see for instance the circled area in Fig. 4(b)) where regular series of proto-fingers appear in some places on both sides of main fingers. This reignition phase lasts until the end of the experiments ($\sim 90\%$ of the experiment time considered in Fig. 4) but is not clearly visible on the map of NaCl 2 M (Fig. 4(d)). Multiple generations of birth and merging can occur around the same primary finger, which contributes to sustain its development over time. Finally, as a consequence of general coarsening, the number of primary fingers decreases in the course of time.

In addition, less frequently, other isolated fingers appear equidistantly from two primary fingers, by contrast to proto-fingers which appear close to them. To avoid confusion between proto-fingers and those new isolated fingers, an example of both types of fingers is highlighted by a circle and by an arrow respectively in Fig. 4(b). The new isolated fingers emerge from a zone at the interface where the velocity is probably low. As a consequence, they are less rapidly absorbed by primary fingers and develop over a certain time before merging. During their development, isolated fingers are sometimes seen to generate a velocity field sufficiently strong to attract momentarily small proto-fingers. These isolated fingers are clearly visible in water (Fig. 4(a)) and Antarctic maps (Fig. 4(b)) where six of them can be observed in the lower part of the image. No statistical analysis could be made on those isolated fingers as too few of them appear over the period of time considered here.

3.3. Wavelengths and reignition time

To better compare the maps of Fig. 4 and assess how salinity impacts the development of the convective fingering, the wavelength λ of fingers at onset is measured by dividing the horizontal length of the map by the number of first fingers counted at the beginning of experiments. In addition, we measure the time interval τ between consecutive finger births in the reignition regime. These results, presented in Table 4, confirm the stabilizing impact of salinity on the convective dynamics.

To begin with, the number of fingers decreases with increasing salinity. The wavelength at onset increases from 4 mm in water to 5.4 mm in NaCl 2 M (Fig. 4(a) and (d) respectively). This effect will be further discussed in Section 4.2.

As a consequence of finger merging, the number of primary fingers sustaining convective motions in the solution is decreasing in the course of time as the wavelength measured at t_{max} (the final time on the space-time maps) is clearly larger than the one measured at onset. This coarsening effect is stronger in more saline solutions as λ at t_{max} in NaCl 2 M is 6 times larger than at the onset of convection, whereas in water λ

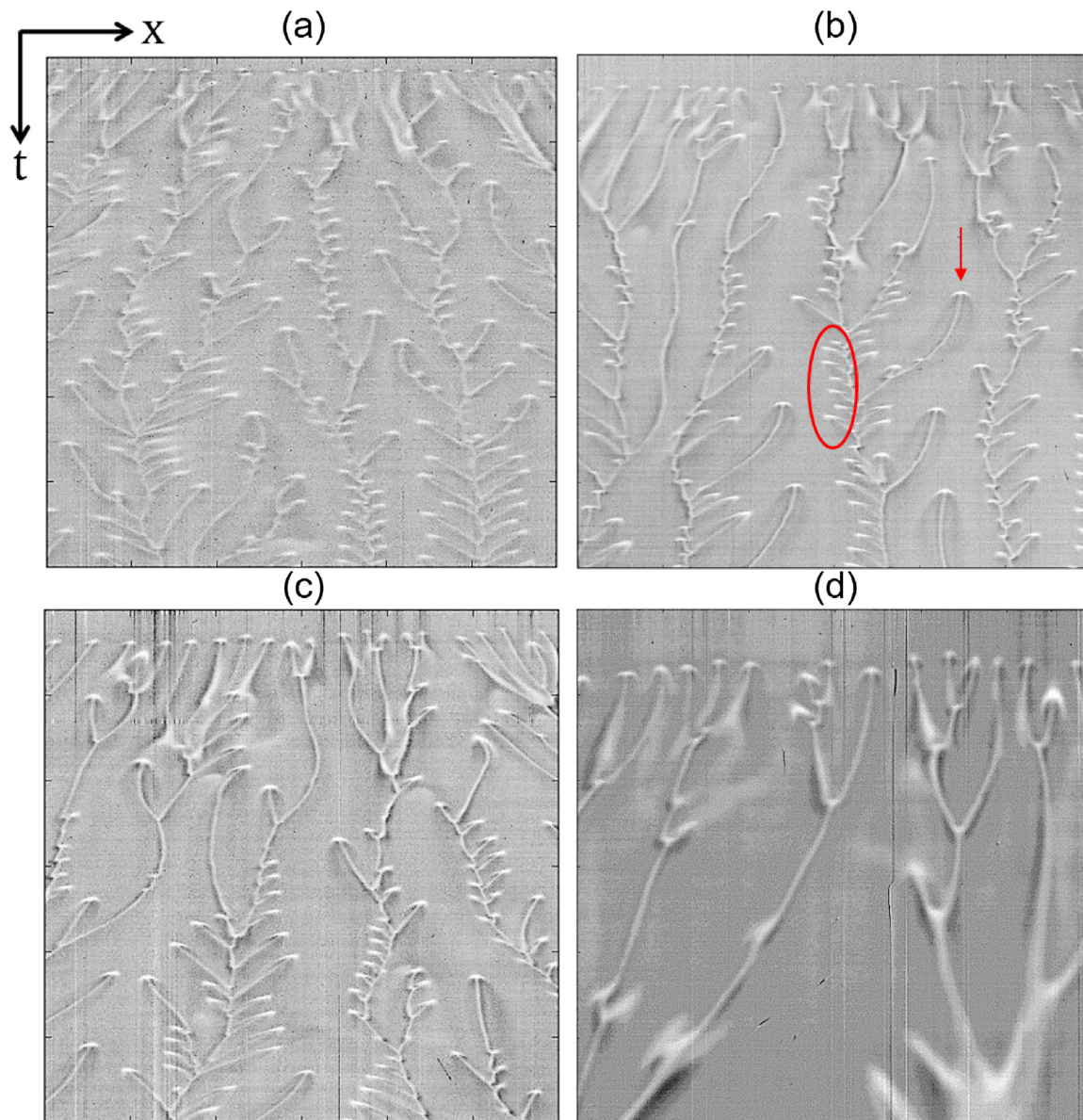


Fig. 4. Comparison of space-time maps of the location of fingers 3 mm below the interface as a function of time in (a) water, (b) Antarctic water and in NaCl (c) 1 M and (d) 2 M solutions. Time is running downwards and the maximum time is 120 min. The horizontal length is 8.7 cm. The time step between two horizontal lines is 10 s. As an example, a regular series of proto-fingers is circled in (b) and the arrow indicates the birth of a new isolated finger.

Table 4

Finger wavelengths λ (mm) at onset and after 2 h of experiment as well as the period τ (s) between birth of proto-fingers as measured on space-time maps of Fig. 4.

Solution	λ onset	λ 120 min	τ proto-fingers
Water	4.0	9.7	205
Antarctic water	4.6	12.4	200
NaCl 1 M	4.3	16.2	208
NaCl 2 M	5.4	29.0	–

only doubles over the course of the experiment.

Finally, the time τ for the development of two successive proto-fingers is roughly the same in water, Antarctic water and NaCl 1 M and is about 200 s. This measure was not possible with NaCl 2 M where proto-fingers are almost absent. Note that those results are obtained for one experiment only and do not correspond to the average of several experiments.

4. Quantitative measurements

Let us now turn to a quantitative characterization of the development of the fingering dynamics.

4.1. Evolution of finger length

4.1.1. Mixing length

In order to characterize the downward progression of the fingers, the vertical length of the mixing zone is measured in the course of time until fingers reach the bottom of the field of view. To do so, gray-level gradients are binarized on the collected images with a Mathematica code to find the tip of the longest finger. The mixing length L is defined as the vertical distance between this tip position and the interface. For each solution considered, the temporal evolution of the mixing lengths L averaged over several experiments is shown in Fig. 5. Note that measurements on binarized pictures is less precise in the diffusive regime where fingers are absent. This regime will be further discussed in

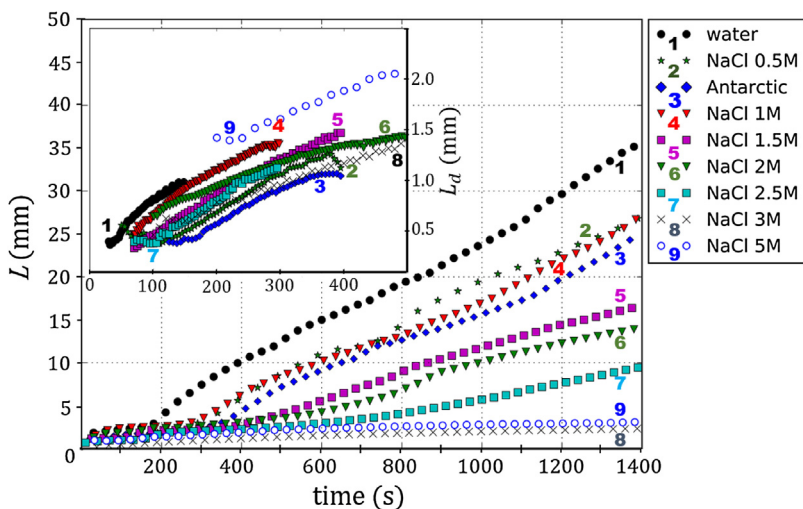


Fig. 5. Temporal evolution of mixing lengths L and diffusive lengths L_d (inset) in water and in saline solutions. Each curve represents the average of several experiments. Averaged standard deviations on L_d in the main panel are 1.7 mm, 1.3 mm, 1.6 mm, 1.7 mm, 1.2 mm, 1.9 mm, 1.4 mm, 0.4 mm and 0.2 mm for water, NaCl 0.5 M, Antarctic water, NaCl 1 M, 1.5 M, 2 M, 2.5 M, 3 M and 5 M, respectively. The equivalent graph with error bars is available in the Supplementary Material. In the insert graph, averaged standard deviations are 0.11 mm, 0.16 mm, 0.13 mm, 0.16 mm, 0.17 mm, 0.45 mm, 0.18 mm, 0.32 mm and 0.37 mm for water, NaCl 0.5 M, Antarctic water, NaCl 1 M, 1.5 M, 2 M, 2.5 M, 3 M and 5 M.

the following section.

In Fig. 5, we see that the development of the instability is similar in all experiments featuring unstable cases. After a characteristic onset time, L departs from its diffusive evolution and increases faster due to the vertical progression of fingers, except for solutions of NaCl 3 M and 5 M which remain in the diffusive regime during the whole course of the experiment (those two curves were computed with another technique described below). In the convective regime, L increases almost linearly over the time period considered here. However, individual fingers do not have a vertical velocity constant over time. Indeed, some fingers can sometimes develop faster than others before they slow down or even stop growing before dying or getting dragged into the flow generated by a neighbouring finger. As we track here the position of the longest finger, this effect can impact the evolution of L which then slows down for some time before it accelerates again. These fluctuations are dampened by averaging L over several experiments but are still visible in Fig. 5.

Fig. 5 shows once again that increasing salinity delays the onset of convection. Moreover, the larger the concentration of salt in the solution, the slower fingers evolve towards the bulk of the solution. This is clearly shown in Fig. 6, which plots the averaged velocity v of fingers as a function of salinity. This is obtained by computing the averaged local slope of the $L(t)$ curves of Fig. 5 in the convective regime. As the characteristic velocity u_c (see Table 3) is proportional to the density difference $\Delta\rho$ and inversely proportional to the viscosity μ , such a decrease in velocity is anticipated as $\Delta\rho$ decreases while μ increases when increasing the salinity. However, the ratio $\Delta\rho/\mu$ computed from Table 3

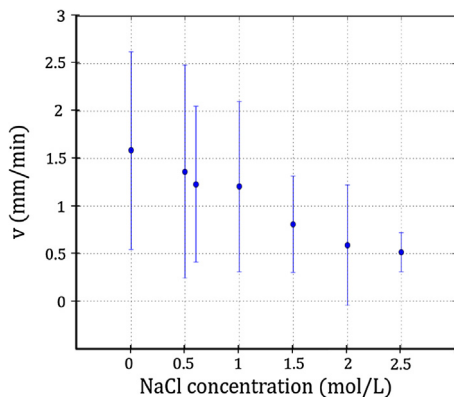


Fig. 6. Averaged velocities of fingers during the convective regime as a function of NaCl concentration. Error bars represent two times standard deviations which correspond to a 95% confidence interval.

only decreases with a factor 2 whereas v is observed to decrease with a factor 3 in Fig. 6. This could be explained by the fact that other effects, such as changes in the critical wavelength, solubility or diffusion coefficient of CO_2 must come into play as well in the dynamics of the system.

Finally, we note that even if the system is more stable in all salted solutions than in water, fingers generated in Antarctic water evolve similarly to the 1 M NaCl solutions, which is more saline than sea water. The Antarctic system is thus more stable than expected as the equivalent concentration of NaCl to Antarctic water is 0.6 M. This effect must be due to the fact that Antarctic water contains other ions than Na^+ and Cl^- which can influence the dynamical properties of the aqueous solution and interfere with the dissolution of CO_2 .

4.1.2. Diffusive length

To follow more precisely the evolution of the diffusive front, pictures were analyzed in detail during the initial time period including the very beginning of the instability. This period of time differs from one solution to another and even represents the whole course of experiment for NaCl 3 M and 5 M. To start with, the coordinates (x,y) of the interface are defined at the beginning of each experiment. Then, the coordinates of the diffusive front generated by CO_2 dissolution are determined on each picture (Fig. 7(a)). The formation of the diffusive front and its subsequent sinusoidal deformation into fingers is followed over time until plumes detach from the interface and start to sink vertically. For each point along x , vertical distances between the interface and the front position are measured. Finally, the mean vertical position L_d of the unstable layer is computed as the averaged value of all vertical distances. Note that this averaged value L_d is *a priori* only relevant in the diffusive regime before the convective modulation starts growing.

Temporal evolutions of L_d are presented on the inset of Fig. 5. Despite the precise detection of the boundary layer growth, no logical order can be found in the evolutions of L_d for the different salinities and averaged standard deviations are large compared to L_d . Indeed, L_d can be found to double from one experiment to another, which leads to a large dispersion of the results. This weak reproducibility is probably due to the fact that even if experiments are performed with the same protocol, a natural variability exists in the initial conditions which strongly affects the development of the diffusive boundary layer. Finally, we note that the diffusive L_d curves of Fig. 5 typically scale as $t^{0.46 \pm 0.09}$ in reasonable agreement with Fick's law of diffusion.

4.2. Fourier analysis

In order to measure the growth rate and wavelength characterizing

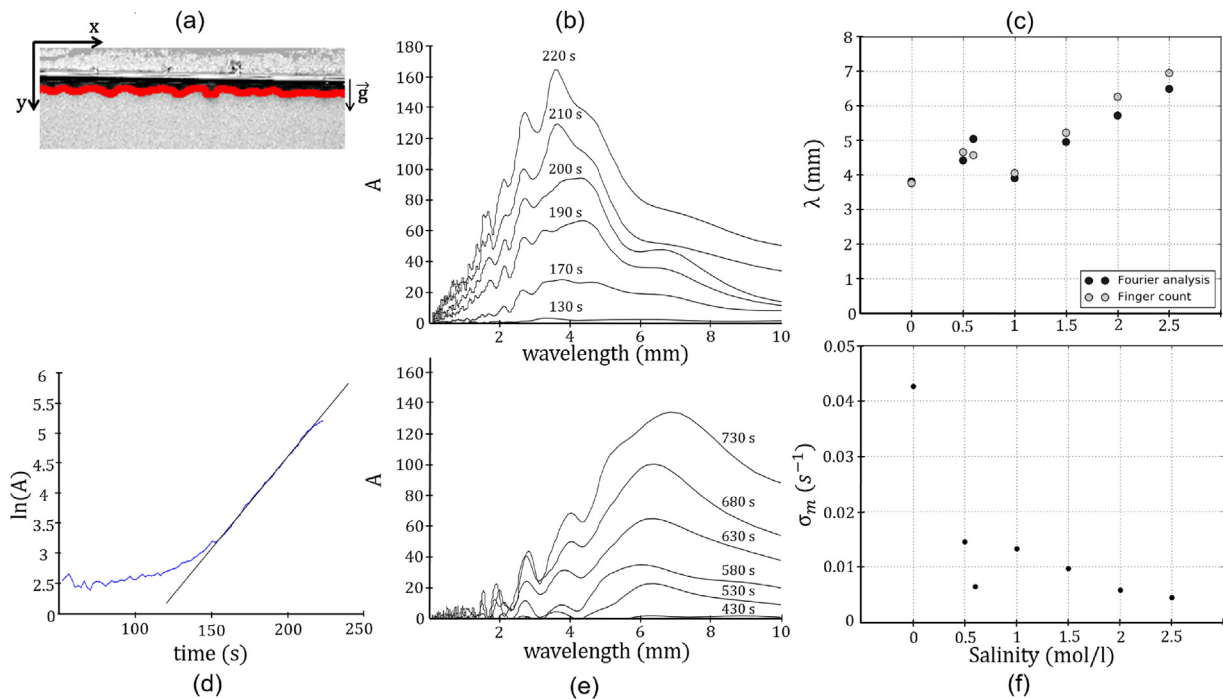


Fig. 7. (a) Example of the detection of the front shape. (b) Temporal evolution of the mean Fourier spectrum of fingers at the onset of convection in water. This dispersion curve gives the amplitude of each mode as a function of its wavelength. Due to the limited sampling and broad spectral peaks, an additional smoothing was applied to each Fourier spectrum to obtain a dominant wavelength which is roughly constant over time. (c) Dependence on salinity of the dominant wavelength computed by Fourier analysis (standard deviations are 0.38 mm, 0.01 mm, 0.03 mm, 0.02 mm, 0.54 mm, 0.78 mm, and 0.6 mm for water, NaCl 0.5 M, Antarctic water, NaCl 1 M, 1.5 M, 2 M, and 2.5 M, respectively) or by counting fingers visually (standard deviations are, in the same order, 0.30 mm, 0.48 mm, 0.59 mm, 0.31 mm, 0.48 mm, 0.95 mm, and 1.01 mm). (d) Temporal evolution of the logarithm of the amplitude of the dominant wavelength of the Fourier spectrum in water. The growth rate σ is computed as the slope of the linear part of the curve. (e) Temporal evolution of the mean Fourier spectrum of fingers at the onset of convection in NaCl 2.5 M. (f) Maximum growth rate σ_m as a function of salinity.

the onset of the convective instability, the progressive deformation of the diffusive front into a sinusoidal pattern was studied by means of Fourier analysis. A fast Fourier transform algorithm was applied to the front shape (Fig. 7(a)) of successive images (Fernandez et al., 2002). The mean Fourier spectrum averaged over several experiments provides dispersion curves i.e. the amplitude of the Fourier mode as a function of the wavelength $\lambda = 2\pi/k$ where k is the wavenumber. Fig. 7(b) and (e) shows the dispersion curves obtained for experiments in water and in a 2.5 M NaCl solutions at different times during the short-time development of convection. Both spectra exhibit a broad distribution with several peaks, the amplitude of which is growing over time with a dominant wavelength at 3.8 mm for water and 6.4 mm for NaCl 2.5 M (see also Table 3).

To compute the characteristic wavelength of fingers at the onset of convection, the wavelength λ_{\max} of the mode of maximum amplitude A_{\max} is averaged in time over the linear regime, i.e. over the time period for which λ_{\max} is roughly constant before the merging of fingers. The salinity dependence of these mean wavelengths computed on the basis of Fourier spectra are compared in Fig. 7(c). The wavelength obtained by simply dividing the horizontal length of the picture by the number of fingers counted visually at the onset of experiment is also given. A fairly good comparison is obtained between both methods. As already observed from the space-time maps of Section 3.2, the wavelength of the fingering pattern increases with increasing concentration of NaCl. The value obtained for Antarctic water seems to be larger than the trend followed by other solutions.

The growth rate σ of each mode is next computed as the slope of the logarithm $\ln(A)$ of its amplitude in Fourier space versus time during the linear regime (Fig. 7(d)). The maximum growth rate σ_m is plotted as a function of salinity in Fig. 7(f). As expected from the stabilizing effect of salinity on convection, σ_m is decreasing in brine of increasing concentration. Here again, the value obtained for Antarctic water is smaller

than in solutions containing higher concentrations of NaCl which corroborate the fact that the presence of other species than NaCl tends to slow down the development of convection.

4.3. Onset time of convection

The time at which the instability initiates in the host phase is frequently computed in theoretical studies because it is particularly important for risk assessment. Indeed, convection enhances the mixing of CO₂ in the brine, increases the dissolution flux and transports CO₂ far away from the interface downwards in the brine. Therefore, the sooner convection arises, the safer the storage process. Various definitions of the onset time can be found in the literature, depending on the method used to study the evolution of the convective dynamics in the host phase. In linear stability analysis, the onset time of convection t^* is most often defined as the time at which the growth rate σ of the most unstable mode switches from negative to positive values, i.e. $\sigma.t^* = 0$ (Ennis-King et al., 2005; Xu et al., 2006; Cheng et al., 2012). Other works have considered the time at which perturbations become significant, i.e. $\sigma.t^* = 1$ (Trevelyan et al., 2011; Loodts et al., 2014b; Slim, 2014). In nonlinear numerical simulations, various definitions of the onset of convection have been suggested, such as the time at which the average CO₂ mass flux at the top boundary has a relative deviation of 1% from a pure diffusive mass flux (Pau et al., 2010). These values are difficult to access experimentally. However, a general scaling for the onset time has been proposed by several studies, which will be further discussed in Section 5.

Experimentally, measuring the onset time as the time at which fingers become visible implies some subjectivity but provides a quick measure of the order of magnitude of this time. Table 5 gives an evaluation of this onset time determined as the time at which the deformation of the diffusive layer becomes observable to the eye. A large

Table 5

Comparison of the onset time (in seconds) of convection evaluated visually, from standard deviation of L_d , and from a superposition of space-time maps.

Solution	Visual	Standard deviation	Space-time maps
Water	142 ± 98	133 ± 72	214 ± 52
NaCl 0.5 M	216 ± 58	213 ± 46	402 ± 66
Antarctic water	254 ± 96	327 ± 82	424 ± 100
NaCl 1 M	188 ± 48	272 ± 80	370 ± 70
NaCl 1.5 M	298 ± 132	396 ± 126	537 ± 156
NaCl 2 M	303 ± 106	450 ± 134	514 ± 260
NaCl 2.5 M	330 ± 160	689 ± 226	643 ± 224

dispersion results from the natural variability of the experiments which is why a minimum of 5 experiments is performed for each salinity. For example, in pure water, 8 experiments have been performed in the same conditions. Convection is seen to arise between 105 s and more than 200 s after the beginning of an experiment. This visual technique is thus not fully reliable particularly in more stable systems where the diffusive layer deforms slowly.

A second more quantitative estimation of the onset time was performed by analyzing the standard deviation of L_d (insert of Fig. 5) measured as the average along the horizontal coordinate x of the vertical distances between the interface and the limit of the mixing zone (see Section 4.1.2). In the diffusive regime, the standard deviation of L_d is small. However, once convection sets in, the vertical distances strongly vary from one position to another along the x axis and the standard deviation increases proportionally to the amplitude of the deformation. As an example, the temporal evolutions of the standard deviations measured for all experiments with NaCl 2.5 M solutions are shown in Fig. 8. For some experiments, the sudden increase of the standard deviation due to the onset of convection is clearly defined but other experiments rather show a progressive increase with no apparent transition. For this reason, we define the onset time as the time at which the standard deviation associated to L_d is equal to 0.1 mm. The resulting averaged onset time obtained with this procedure is provided in the second column of Table 5. Note that this method is reliable only if the diffusive front and its destabilization are precisely detected.

A third approach consists in detecting the averaged time at which first fingers appear on the space-time maps studied in Section 3.2. To do so, the space-time maps of all experiments at a given salinity are combined on one same image (see example in Fig. 9) and the averaged time at which fingers appear is inferred. The onset times obtained with this last method are shown in the last column of Table 5. Their values is typically larger than with the visual or L_d standard deviation techniques as the time measured is the one when fingers reach a depth of 2 mm below the interface and not when they appear. Moreover, this time depends on the velocity of fingers, which is influenced by the salt concentration in the aqueous solution while the gas–liquid interface is sometimes not entirely horizontal but can be slightly tilted and/or

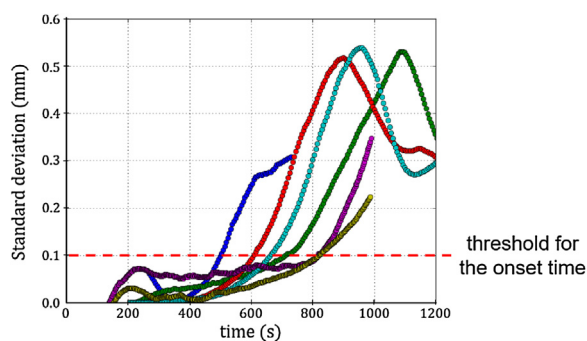


Fig. 8. Temporal evolution of the standard deviation associated to the average of the diffusive length L_d in the experiments of NaCl 2.5 M. The onset time in this case is defined as the time at which the standard evolution reaches 0.1 mm.

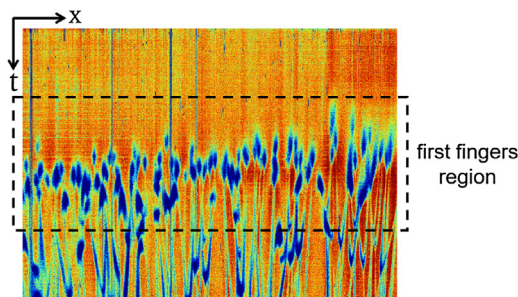


Fig. 9. Superposition of all the space-time maps obtained for experiments in solutions of NaCl 0.5 M at 2 mm below the interface. The maximum time is 800 s.

present irregularities in the vertical direction. In that case, the distance between the interface and the position of the line selected for the space-time map is not exactly 2 mm in all points along x . Consequently, the error on the values obtained with this method is large.

We thus see that the experimental values of convection onset times depend on the method used. However, orders of magnitude remain similar and the conclusion is the same for all three methods, i.e. convection is delayed when the salt concentration is increased.

5. Discussion

5.1. Comparison with previous experiments

Very few experiments have characterized the development of convective fingers upon dissolution of CO_2 in water or NaCl solutions in terms of characteristic onset time, wavelength, growth rate and velocity. In water, Kneafsey and Pruess (2010) evaluated visually using a color indicator an onset time of convection of approximately 3 min, similar to what is observed here, and the wavelength at onset time was observed to be 10 mm, which is considerably larger than all the wavelengths measured here. In a similar study with color indicator, Faisal et al. showed that convection can be detected visually in the aqueous layer after approximately 30 s (Faisal et al., 2013) or 60 s (Faisal et al., 2015). These discrepancies are not surprising as the gap width of the Hele–Shaw cell used in Kneafsey and Pruess (2010) is smaller than here (0.7 mm), and is non uniform across the length of the cell (larger gap at the center) in Faisal et al. (2013, 2015) so the Rayleigh numbers characterizing these systems are different from ours, which strongly impact the wavelength and onset time of the fingering pattern. Moreover, the injection method of gases used by Kneafsey and Pruess or Faisal et al. is very different than the one chosen here, which can impact the early development of fingers.

Outeda et al. (2014) who also used a color indicator visualization technique (but inject N_2 before CO_2 in a Hele–Shaw cell of gap width of 1 mm like we do here) obtain a growth rate between 0.15 s^{-1} to 0.36 s^{-1} and a wavenumber of the order of 19 cm^{-1} (i.e. $\lambda = 2\pi/k = 3.3 \text{ mm}$) when varying concentrations of the color indicator and pressures. The growth rate is larger than our value $\sigma_m = 0.042 \text{ s}^{-1}$ while the wavelength is slightly smaller than ours (3.8 mm). A possible source of discrepancy might be that higher pressures are used by Outeda et al. (2014).

A comparison with the results of Vreme et al. (2016) who have measured convective dissolution of CO_2 in pure water can be performed as well. Their visualization involves fluorescein and PIV tracers but they have checked that their results are unchanged when varying the concentration of fluorescein over 3 orders of magnitude. A specific injection device ensures CO_2 injection without any pressure change. They have scanned a wide range of Rayleigh numbers by varying the gas pressure and the gap width of the cell. Our Rayleigh number R_a defined by Eq. (1) i.e. constructed on the basis of the gap width a of the cell

corresponds to the parameter denoted $Ra\sqrt{Da}$ in their study. For our experiment in pure water with Ra of the order of 39, we obtain $\sigma = 0.042 \text{ s}^{-1}$ (Fig. 7(f)) and $\lambda = 3.8 \text{ mm}$ (Fig. 7(c)) which, along with $t_c = 0.031 \text{ s}$ and $l_c = 7.35 \cdot 10^{-6} \text{ m}$ (Table 3) give a dimensionless growth rate $\sigma^* = 0.0013$ and dimensionless wavenumber $q^* = 0.012$. This compares favorably with the values $q^* = 0.0005$ (Fig. 5b of Vreme et al., 2016) and $q^* = 0.015$ (Fig. 6b of Vreme et al., 2016). This indicates that our experiments are most likely in the Darcy-Brinkman regime as concluded from Vreme et al.'s results.

If we consider the experimental studies performed in PVT cells where the effect of salinity was studied, our results corroborate the fact that convection is weakened in highly concentrated brine. In particular, the studies by Farajzadeh et al. (2007) and Khosrokhavar et al. (2014) showed that the rate of the mass transfer of CO_2 is decreased if the concentration of NaCl in the solution is increased, which is in agreement with our observations. The novelty of our results is to highlight the changes in growth rates and wavelengths of the fingering patterns when salinity is changed, which is not possible to access in PVT cells.

5.2. Comparison with theoretical predictions

5.2.1. Influence of the salt concentration

Recently, on the basis of a linear stability analysis and Darcy's law, Loodts et al. (2014b) have predicted that increasing salinity stabilizes the convective dissolution of CO_2 in aqueous solutions of NaCl. Our experimental results are in perfect qualitative agreement with this theoretical work. Loodts et al. have interpreted the stabilizing effect of salt concentration by its impact on several physical quantities influencing the time and length scales characterizing the dynamics. First, the solubility A_0 of CO_2 in the aqueous solution decreases with the concentration of salt, which decreases the density gradient $\Delta\rho$ at the origin of the instability (cf Table 3). Second, the viscosity of the brine increases with salt concentration which also stabilizes the system. Third, the diffusion coefficient of CO_2 decreases when salt is added in the aqueous solution which tends to destabilize the system but this last effect is minor compared to the stabilizing effect of solubility and viscosity.

Quantitatively, a direct comparison between our results and the theoretical values of the maximum growth rate σ_m or the wavelength λ of fingers computed by Loodts et al. (2014b) is difficult. First of all, their values are calculated in the Darcy regime while we are rather in the Darcy-Brinkman domain. Their results are obtained for a gap width of 0.5 mm (half of our value) and their maximum growth rate σ_m is computed at a time t^* for which $\sigma.t^* = 1$ whereas we compute a growth rate averaged over the entire linear regime. To sum up, Loodts et al. found a wavelength increase from 2.7 mm to 4.7 mm for 0 M to 5 M NaCl concentrations and a gap of 0.5 mm whereas we find an increase from 3.8 mm to 6.4 mm for 0 M to 2.5 M and stabilization for larger salinities in our cell of 1 mm gap width.

5.2.2. Characteristic parameters of the convective instability

To further compare our experimental results with theoretical studies, we analyze the dimensionless onset time of convection t_{onset}^* suggested by Ennis-King and Paterson (Ennis-King and Paterson, 2005):

$$t_{\text{onset}}^* = \frac{t_{\text{onset}}}{t_c} = t_{\text{onset}} \frac{(\Delta\rho g \kappa)^2}{\mu^2 \phi^2 D_{\text{CO}_2}} \quad (2)$$

In water, our measured onset time of the order of 140 s along with a characteristic time $t_c = 0.031 \text{ s}$ gives $t_{\text{onset}}^* = 4516$ of the order of the observation time t_{NL} measured by Vreme et al. (Fig. 7b of Vreme et al. (2016)).

In the literature, depending on the theoretical method and the definition of the onset time, a large range of t_{onset}^* values is found (Ennis-King and Paterson, 2005; Riaz et al., 2006; Rees et al., 2008; Pau et al., 2010; Kneafsey and Pruess, 2011; Cheng et al., 2012; Faisal et al., 2013;

Tilton et al., 2013; Emami-Meybodi et al., 2015). When compared with linear stability analysis (LSA) results, our value of t_{onset}^* is roughly 25 times larger than the largest value predicted (Emami-Meybodi et al., 2015). On the contrary, in nonlinear simulations, closer values between 1000 and 5000 depending on the noise and integration technique are found when comparing to the time at which the dissolution flux begins to grow and fingers become visible (Elenius and Johannsen, 2012; Emami-Meybodi et al., 2015; Rasmusson et al., 2017). Finally, Elenius and Johannsen (2012) also found in the nonlinear regime a characteristic finger vertical velocity of about 1.2 mm/min, which is in good agreement with the 1.6 mm/min averaged velocity computed in this study for pure water.

A similar scaling has been proposed for the dimensionless critical wavenumber k^* of the instability at the onset of convection defined as:

$$k^* = \frac{k}{l_c} = k \frac{\Delta\rho g \kappa}{D_0 \phi \mu} \quad (3)$$

In this case, we find values of k^* ranging from 0.012 in water to 0.008 in NaCl 2M whereas LSA typically predicts values for water which are 4 to 6 times larger (Emami-Meybodi et al., 2015), meaning that the predicted wavelengths in theoretical studies are smaller than in experiments.

We note that all these theoretical predictions are based on Darcy's law and it is expected that the use of a Darcy-Brinkman model should improve the comparison especially for the dimensionless wavenumber prediction (Vreme et al., 2016). However, the typical dimensionless onset times computed in LSA are systematically an order of magnitude too small when compared with our experimental results. This inconsistency between LSA and experiments has already been reported by Taheri et al. (2012) who suggest that LSA techniques compute properties of fingers before they become visible to the eye. Therefore, it appears that only nonlinear simulations are able to determine the time at which the deformation reaches a macroscopic size and becomes observable in laboratory-scale experiments. In particular, an onset time defined as the time at which the dissolution flux begins to grow and fingers become visible gives better agreement with experiments. Yet, precise quantitative comparison with experiments will remain difficult as this onset time depends on the properties of the noise seeding the instability which is difficult to apprehend experimentally.

6. Conclusion

We have provided a detailed experimental characterization of the spatio-temporal evolution of the buoyancy-driven convective fingering generated by CO_2 dissolution in water, Antarctic water and in solutions containing NaCl with concentrations up to 5 M. Experiments to visualize the fingering pattern developing in the aqueous phase were conducted at ambient conditions in a vertical Hele-Shaw cell with a schlieren imaging set-up. To the best of our knowledge, this is the first time that CO_2 convective dissolution is observed in water and salt solutions in a spatially extended system at ambient conditions with an optical imaging system in absence of any dye and any chemical reaction. Space-time maps of the location of finger bases were analyzed to characterize the dynamics of finger movements and births near the interface. We have measured the evolution of the mixing length as a function of time and have determined the characteristic velocity of fingers sinking in water or in brine. We have also analyzed the growth of the diffusive layer preceding the onset of convection. By performing a Fourier analysis of the spatial deformation by convection of the diffusive front, we have determined experimentally characteristic wavelengths, growth rates and onset times for CO_2 convective dissolution in pure water and in brine of different salinities.

In agreement with theoretical predictions we find that an increase of salinity of the host phase weakens convection developing upon dissolution of CO_2 . Indeed, increasing the NaCl concentration delays the time at which fingers appear, increases their wavelength, and decreases

the growth rate of the convective instability. In solutions containing high concentrations of NaCl (3 M and 5 M), no convection was observed. Furthermore, we showed that fingers interact less in brine than in water and that less fingers are produced over time in concentrated brine. We noted also that the results obtained in Antarctic water do not follow the same trend as in NaCl solutions as the system is more stable than expected for an equivalent NaCl concentration. Practically, this means that the measure of the salinity only is not sufficient to predict mixing times of CO₂ dissolution in a given aquifer because the presence of other species than NaCl impacts the development of convection. This is coherent with our recent study showing that the very nature of counter-ions is important in quantifying the time and length scales of convective dissolution (Thomas et al., 2016). It shows that knowing the exact composition and reactivity of an aquifer is an important prerequisite to predict its storage capacity. This also means that some aquifers might have a better storage capacity than others, depending on their salt composition.

The direct comparison of our experimental results with theoretical predictions shows that key quantitative characteristics of the convective dynamics such as the onset time of the instability are smaller in LSA studies than in experiments. Results from nonlinear simulations compare better on a quantitative point of view even if the unknown dependence on the initial noise remains an issue. This calls for further studies devoted to benchmark theoretical work and numerical simulations with laboratory experiments. This is a prerequisite before being able to use these models to predict field scale CCS capacities at higher pressures and temperatures. In this regard, we hope that the present detailed experimental results will help towards this goal.

Acknowledgements

We thank F. Brau, P. Bunton, V. Hallet, V. Loodts, L. Rongy and G. Schuszter for fruitful discussions, and J.-L. Tison and B. Delille for the supply and salinity measurement of Antarctic water samples. Funding by the ARC CONVINCE, and PDR-FNRS FORECAST projects is gratefully acknowledged.

Appendix A. Supplementary data

Supplementary data associated with this article can be found, in the online version, at [10.1016/j.ijggc.2018.01.019](https://doi.org/10.1016/j.ijggc.2018.01.019)

References

- Almarcha, C., Trevelyan, P.M.J., Riolfo, L.A., Zalts, A., El Hasi, C., D'Onofrio, A., De Wit, A., 2010. Active role of a color indicator in buoyancy-driven instabilities of chemical fronts. *J. Phys. Chem. Lett.* 1, 752–757.
- Backhaus, S., Turitsyn, K., Ecke, R.E., 2011. Convective instability and mass transport of diffusion layers in a Hele–Shaw geometry. *Phys. Rev. Lett.* 106, 104501.
- Bour, O., Thoraval, A., 2010. Etat de l'art et analyse des risques pour un stockage de CO₂ en aquifère salin. INERIS report DRS-10-100887-12619A.
- Cheng, P., Besthorn, M., Firoozabadi, A., 2012. Effect of permeability anisotropy on buoyancy-driven flow for CO₂ sequestration in saline aquifers. *Water Resour. Res.* 48, W09539.
- Elenius, M.T., Johannsen, K., 2012. On the time scales of nonlinear instability in miscible displacement porous media flow. *Comput. Geosci.* 16, 901–911.
- Emami Meybodi, H., Hassanzadeh, H., 2013. Mixing induced by buoyancy-driven flows in porous media. *AIChE J.* 59, 1378–1389.
- Emami-Meybodi, H., Hassanzadeh, H., Green, C.P., Ennis-King, J., 2015. Convective dissolution of CO₂ in saline aquifers: progress in modeling and experiments. *Int. J. Greenh. Gas Control* 40, 238–266.
- Emami-Meybodi, H., 2017. Stability analysis of dissolution-driven convection in porous media. *Phys. Fluids* 29, 014102.
- Ennis-King, J., Paterson, L., 2002. Engineering aspects of geological sequestration of carbon dioxide. SPE 77809, Proceedings of the SPE Asia Pacific Oil and gas conference and exhibition, Melbourne, Australia 1–13.
- Ennis-King, J., Paterson, L., 2005. Role of convective mixing in the long-term storage of carbon dioxide in deep saline formations. *SPE J.* 10, 349–356.
- Ennis-King, J., Preston, I., Paterson, L., 2005. Onset of convection in anisotropic porous media subject to a rapid change in boundary conditions. *Phys. Fluids* 17, 084107.
- Faisal, T.F., Chevalier, S., Sassi, M., 2013. Experimental and numerical studies of density driven natural convection in saturated porous media with application to CO₂ geological storage. *Energy Proc.* 37, 5323–5330.
- Faisal, T.F., Chevalier, S., Bernabe, Y., Juanes, R., Sassi, M., 2015. Quantitative and qualitative study of density driven CO₂ mass transfer in a vertical Hele–Shaw cell. *Int. J. Heat Mass Transf.* 81, 901–914.
- Farajzadeh, R., Barati, A., Delil, H.A., Bruining, J., Zitha, P.L.J., 2007. Mass transfer of CO₂ into water and surfactant solutions. *Petrol. Sci. Technol.* 25, 1493–1511.
- Farajzadeh, R., Zitha, P.L.J., Bruining, J., 2009. Enhanced mass transfer of CO₂ into water: experiment and modeling. *Ind. Eng. Chem. Res.* 48, 6423–6431.
- Fernandez, J., Kurowski, P., Petitjeans, P., Meiburg, E., 2002. Density-driven unstable flows of miscible fluids in a Hele–Shaw cell. *J. Fluid Mech.* 451, 239–260.
- Firoozabadi, A., Cheng, P., 2010. Prospects for subsurface CO₂ sequestration. *AIChE J.* 56, 1398–1405.
- Hassanzadeh, H., Pooladi-Darvish, M., Keith, D.W., 2005. Modeling of convective mixing in CO₂ storage. *J. Can. Pet. Technol.* 44, 43–51.
- Hassanzadeh, H., Pooladi-Darvish, M., Keith, D.W., 2006. Stability of a fluid in a horizontal saturated porous layer: effect of non-linear concentration profile, initial, and boundary conditions. *Transp. Porous Med.* 65, 193–211.
- Hassanzadeh, H., Pooladi-Darvish, M., Keith, D.W., 2007. Scaling behavior of convective mixing, with application to geological storage of CO₂. *AIChE J.* 53, 1121–1131.
- Hidalgo, J.J., Fe, J., Cueto-Felgueroso, L., Juanes, R., 2012. Scaling of convective mixing in porous media. *Phys. Rev. Lett.* 109, 264503.
- International Energy Agency, 2016. 20 years of carbon capture and storage, accelerating future deployment. OECD/IEA report.
- Karimaie, H., Lindeberg, E., 2017. Experimental verification of CO₂ dissolution rate due to diffusion induced convection. *Energy Proc.* 114, 4917–4925.
- Khosrokhavar, R., Elsinga, G., Farajzadeh, R., Bruining, H., 2014. Visualization and investigation of natural convection flow of CO₂ in aqueous and oleic systems. *J. Pet. Sci. Eng.* 122, 230–239.
- Kneafsey, T.J., Pruess, K., 2010. Laboratory flow experiments for visualizing carbon dioxide-induced, density-driven brine convection. *Transp. Por. Med.* 82, 123–139.
- Kneafsey, T.J., Pruess, K., 2011. Laboratory experiments and numerical simulation studies of convectively enhanced carbon dioxide dissolution. *Energy Proc.* 4, 5114–5121.
- Kuster, S., Riolfo, L.A., Zalts, A., El Hasi, C., Almarcha, C., Trevelyan, P.M.J., De Wit, A., D'Onofrio, A., 2011. Differential diffusion effects on buoyancy-driven instabilities of acid–base fronts: the case of a color indicator. *Phys. Chem. Chem. Phys.* 13, 17295–17303.
- Loodts, V., Thomas, C., Rongy, L., De Wit, A., 2014a. Control of convective dissolution by chemical reactions: general classification and application to CO₂ dissolution in reactive aqueous solutions. *Phys. Rev. Lett.* 113, 114501.
- Loodts, V., Rongy, L., De Wit, A., 2014b. Impact of pressure, salt concentration, and temperature on the convective dissolution of carbon dioxide in aqueous solutions. *Chaos* 24, 043120.
- Loodts, V., Knaepen, B., Rongy, L., De Wit, A., 2017. Enhanced steady-state dissolution flux in reactive convective dissolution. *Phys. Chem. Chem. Phys.* 19, 18565.
- MacMinn, C.W., Juanes, R., 2013. Buoyant currents arrested by convective dissolution. *Geophys. Res. Lett.* 40, 2017–2022.
- Metz, B., Davidson, O., de Coninck, H.C., Loos, M., Meyer, L.A., 2005. IPCC special report on carbon dioxide capture and storage. In: Prepared by working group III of the Intergovernmental Panel on Climate Change. Cambridge University Press.
- Neufeld, J.A., Hesse, M.A., Riaz, A., Hallworth, M.A., Tchelepi, H.A., Huppert, H.E., 2010. Convective dissolution of carbon dioxide in saline aquifers. *Geophys. Res. Lett.* 37, L22404.
- Outeda, R., El Hasi, C., D'Onofrio, A., Zalts, A., 2014. Experimental study of linear and nonlinear regimes of density-driven instabilities induced by CO₂ dissolution in water. *Chaos* 24, 013135.
- Pachauri, R.K., Meyer, L.A., 2014. Climate Change 2014: Synthesis report, summary for policymakers. In: Contribution of Working Group I, II and III to the Fifth Assessment Report of the Intergovernmental Panel on Climate Change. Cambridge University Press, IPCC Geneva, Switzerland.
- Pau, G.S.H., Bell, J.B., Pruess, K., Almgren, A.S., Lijewski, M.J., Zhang, K., 2010. High-resolution simulation and characterization of density-driven flow in CO₂ storage in saline aquifers. *Adv. Water Resour.* 33, 443–455.
- Rasmusson, M., Fagerlund, F., Rasmusson, K., Tsang, Y., Niemi, A., 2017. Refractive-Light-Transmission technique applied to density-driven convective mixing in porous media with implications for geological CO₂ storage. *Water Resources Res.* 53, 8760–8780.
- Rees, D.A.S., Selim, A., Ennis-King, J.P., 2008. The stability of unsteady boundary layers in porous media. In: Vadasz, P. (Ed.), *Emerging Topics in Heat and Mass Transfer in Porous Media, Theory and Applications of Transport in Porous Media*, vol. 22. Springer, Netherlands, pp. 85 (chapter 4).
- Riaz, A., Hesse, M., Tchelepi, H.A., Orr Jr., F.M., 2006. Onset of convection in a gravitationally unstable, diffusive boundary layer in porous media. *J. Fluid Mech.* 548, 87–111.
- Sell, A., Fadaei, H., Kim, M., Sinton, D., 2013. Measurement of CO₂ diffusivity for carbon sequestration, A microfluidic approach for reservoir-specific analysis. *Environ. Sci. Technol.* 47, 71–78.
- Settles, G.S., 2001. *Schlieren and Shadowgraph Techniques: Visualizing Phenomena in Transparent Media*. Springer-Verlag.
- Seyyedi, M., Rostami, B., Nazari-Moghaddam, R., Rezaei, M., 2014. Experimental study of density-driven convection effects on CO₂ dissolution rate in formation water for geological storage. *J. Nat. Gas Sci. Eng.* 21, 600–607.
- Slim, A.C., Bandi, M.M., Miller, J.C., Mahadevan, L., 2013. Dissolution-driven convection in a Hele–Shaw cell. *Phys. Fluids* 25, 024101.
- Slim, A.C., 2014. Solutal-convection regimes in a two-dimensional porous medium. *J. Fluid Mech.* 741, 461–491.
- Soroush, M., Wessel-Berg, D., Torsaeter, O., Taheri, A., Kleppe, J., 2012. Affecting

- parameters in density driven convection mixing in CO₂ storage in brine. In: SPE-154901, SPE Europec/EAGE Annual Conference. Copenhagen, Denmark.
- Taheri, A., Torsaeter, O., Wessel-Berg, D., Soroush, M., 2012. Experimental and simulation studies of density-driven-convection mixing in a Hele–Shaw geometry with application for CO₂ sequestration in brine aquifers. In: SPE-154908, SPE Europec/EAGE Annual Conference. Copenhagen, Denmark.
- Tilton, N., Daniel, D., Riaz, A., 2013. The initial transient period of gravitationally unstable diffusive boundary layers developing in porous media. *Phys. Fluids* 25, 092107.
- Thomas, C., Lemaigre, L., Zalts, A., D’Onofrio, A., De Wit, A., 2015. Experimental study of CO₂ convective dissolution: the effect of color indicators. *Int. J. Greenh. Gas Control* 42, 525–533.
- Thomas, C., Loodts, V., Rongy, L., De Wit, A., 2016. Convective dissolution of CO₂ in reactive alkaline solutions: Active role of spectator ions. *Int. J. Greenh. Gas Control* 53, 230–242.
- Thomas, C., 2017. Influence of chemical reactions on CO₂ convective dissolution: an experimental study. Ph. D. thesis, Université libre de Bruxelles, Brussels, Belgium.
- Trevelyan, P.M.J., Almarcha, C., De Wit, A., 2011. Buoyancy-driven instabilities of miscible two-layer stratifications in porous media and Hele–Shaw cells. *J. Fluid Mech.* 670, 38–65.
- Tsai, P.A., Riesing, K., Stone, H.A., 2013. Density-driven convection enhanced by an inclined boundary: implications for geological CO₂ storage. *Phys. Rev. E* 87, 011003.
- Vreme, A., Nadal, F., Pouligny, B., Jeandet, P., Liger-Belair, G., Meunier, P., 2016. Gravitational instability due to the dissolution of carbon dioxide in a Hele–Shaw cell. *Phys. Rev. Fluids* 1, 064301.
- Wylock, C., Dehaeck, S., Cartage, T., Colinet, P., Haut, B., 2011. Experimental study of gas–liquid mass transfer coupled with chemical reactions by digital holographic interferometry. *Chem. Eng. Sci.* 66, 3400–3412.
- Wylock, C., Rednikov, A., Haut, B., Colinet, P., 2014. Nonmonotonic Rayleigh–Taylor instabilities driven by gas–liquid CO₂ chemisorption. *J. Phys. Chem. B* 118, 11323–11329.
- Xu, X., Chen, S., Zhang, D., 2006. Convective stability analysis of the long-term storage of carbon dioxide in deep saline aquifers. *Adv. Water Resour.* 29, 397–407.
- Yang, C., Gu, Y., 2006. Accelerated mass transfer of CO₂ in reservoir brine due to density-driven natural convection at high pressures and elevated temperatures. *Ind. Eng. Chem. Res.* 45, 2430–2436.